

Pump-cavity synchronization mismatch in modulation instability induced optical frequency combsStefano Negrini , Saliya Coulibaly, François Copie , Majid Taki, and Arnaud Mussot ^{*}
Université Lille, CNRS, UMR 8523, PhLAM - Physique des Lasers Atomes et Molécules, F-59000 Lille, France

(Received 9 December 2022; accepted 21 February 2023; published 30 May 2023)

We report the observation of the frequency shift of modulation instability sidelobes due to the synchronization mismatch between the pulsed pump period and the resonator's round-trip time. We show that a very small synchronization mismatch leads to a significant frequency shift of the modulation instability sidelobes. We develop a theory originating from absolute and convective instabilities to confirm experimental observations and numerical simulations. The temporal drifts of the Turing patterns induced by the synchronization mismatch are measured in real time using a time-lens system and confirm theoretical predictions.

DOI: [10.1103/PhysRevResearch.5.023133](https://doi.org/10.1103/PhysRevResearch.5.023133)**I. INTRODUCTION**

Optical frequency combs have attracted a lot of attention these last years because they revolutionized ultraprecise frequency measurements in many applications such as spectroscopy, wavelength division multiplexing, lidar, or optical clocks to name a few [1,2]. The development of high-quality factor microresonators made from highly nonlinear materials enables a huge enhancement of nonlinear effects within these small chips. They made possible the continuous-wave (cw) pumping of a few mW only to generate wideband optical frequency combs (OFCs) with potentially on-chip integrated lasers, which makes them very appealing for many applications [2]. Thus, most works have been achieved using cw pumps. However, while more cumbersome and requiring a fine synchronization with the cavity, pulsed pump configurations enable a much higher conversion efficiency of the pump into the OFC [3–5]. The drawback is that an almost perfect synchronization must be implemented, otherwise the OFC coherence and stability may be degraded [6–9]. Synchronization mismatch can also induce unexpected bifurcations and/or asymmetry in OFCs [10–12]. Practically, the free spectral range of the cavity must be equal to the pump repetition rate (an exact integer [13]) in order to coherently drive the cavity. This requires pump laser sources with high stability and a fine tuning of the repetition rate of the order of tens of Hz. Thus, it is of great interest to study the impact of synchronization mismatch of the primary stage of cavity optical frequency combs which is governed by the modulation instability (MI) process dynamics [1]. We remind MI refers to the destabilization of two symmetric sidebands around the pump resulting from an interplay between nonlinearity,

dispersion, and periodic boundary conditions of the cavity [14]. In the simplest configuration, i.e., cw pumping, for large group velocity dispersion, pump power just above the cavity threshold, the position of these bands is ruled by a phase-matching relation, including the Kerr effect, cavity detuning, and second-order dispersion term [14,15]. In weak dispersion regimes, the spectra are broader and higher-order dispersion terms must be accounted for accurately to describe the dynamics of the process. Even orders only explicitly appear in the phase-matching relation and contribute to a modification of the position and/or the destabilization of a new set of sidebands [16–18]. The contribution of higher-order odd-dispersion terms can become significant by inducing a symmetry breaking in the system, leading to drift instabilities in the time domain. Thus, a competition between amplification and drift processes occurs, which is referred to as convective instabilities, a widespread phenomenon investigated in numerous nonlinear physical systems [19–23]. In optical fiber resonators, the third-order dispersion contribution leads to a symmetry breaking of the MI process [23,24], as well as a modification of the bifurcation dynamics [25]. Regarding the contribution of the lower odd-order dispersion term which corresponds to the synchronization mismatch between the pump and the resonator, it has been reported to alter the dynamics [26]. However, no significant modification of the sideband position, which is a fundamental signature of the MI process, had been reported so far. In this paper, we show that in the pulsed pump-driven passive resonators the synchronization mismatch between the pump and the cavity leads to a significant modification of the MI sideband position. In other words, we show that the first-order dispersion term modifies the position of the MI sidelobes, whereas it should play no role based on the standard linear stability analysis, where only even-numbered terms should be considered in the phase-matching relation [14,15].

II. THEORY

We based our theoretical investigations on the Lugiato-Lefever equation (LLE) including a gradient term $\Delta\beta_1\partial E/\partial\tau$

^{*}arnaud.mussot@univ-lille.fr

Published by the American Physical Society under the terms of the Creative Commons Attribution 4.0 International license. Further distribution of this work must maintain attribution to the author(s) and the published article's title, journal citation, and DOI.

[27] to account for the synchronization mismatch,

$$i \frac{\partial E(z, \tau)}{\partial z} + i \Delta \beta_1 \frac{\partial E}{\partial \tau} - \frac{\beta_2}{2} \frac{\partial^2 E(z, \tau)}{\partial \tau^2} + \gamma |E(z, \tau)|^2 E(z, \tau) = i \frac{\theta}{L} E_{\text{in}} + \left(\frac{\delta_0}{L} - i \frac{\alpha}{L} \right) E, \quad (1)$$

where z is the propagation distance [$mL < z < (m+1)L$ corresponds to the round trip m], τ is the time in the laboratory reference frame, and $E(z, \tau)$ is the intracavity electric field. The parameters L , γ , and β_2 correspond to the cavity length, the nonlinear coefficient, and the group velocity dispersion of the fiber, respectively. The quantity $\Delta \beta_1 = \frac{t_R - t_{R,0}}{L}$, with t_R the period of the input pulse train and $t_{R,0} = nL/c$ the round-trip time of the cavity, refers to the synchronization mismatch. The parameters θ and ρ define the transmission and reflection coefficients of the coupler such that $\theta^2 + \rho^2 = 1$. The constant α accounts for the overall losses (splices, coupling, linear losses, and excess loss of the coupler) over a cavity round trip, and δ_0 is the cavity detuning [14]. We checked numerically that the contribution of higher-order linear and nonlinear terms is negligible in the experimental system under consideration. The LLE has a homogeneous steady solution (HSS) given by $E_s = \sqrt{I_s} e^{i\phi_s}$ such that $S^2 - I_s[\alpha^2 + (\delta - I_s)^2] = 0$ and $\phi_s = -\arctan \frac{\delta - I_s}{\alpha}$. The linear stability analysis of this solution with respect to a perturbation of the form $e^{i(\omega\tau - \lambda z)}$ yields the following dispersion relation,

$$D(\lambda, \omega) \equiv (\lambda - \Delta \beta_1 \omega + i\alpha)^2 + [I_s^2 - (\omega^2 + \delta - 2I_s)^2]. \quad (2)$$

The HSS is stable if the imaginary part of the following λ solution is negative,

$$\lambda(\omega) = \Delta \beta_1 \omega + i \left[-\alpha + \sqrt{I_s^2 - (\omega^2 + \delta - 2I_s)^2} \right]. \quad (3)$$

The frequency shift of the MI $\omega_{\text{MI}} = \sqrt{2I_s - \delta}$ is then obtained by solving the equation $\text{Im}(\partial_\omega \lambda) = 0$. The corresponding phase velocity $v_\phi = \text{Re}(\lambda)/\omega = \Delta \beta_1$. It is also known [28,29] that for a localized perturbation, the linear stability analysis must be considered through the determination of the linear response. More precisely, it is the asymptotic properties of this solution in a reference frame moving with the pseudovelocity b_1 with respect to the absolute frame, that is, $\tau = \tau_0 + b_1 z$, where τ_0 is fixed. In practice, setting $S(\lambda, \omega)$, the function representing the initial perturbation, the linear solution reads

$$E_{\text{lin}}(\tau_0 + b_1 z, z) = \int_{-\infty}^{\infty} d\omega \int_{i\sigma - \infty}^{i\sigma + \infty} \frac{S(\lambda + \Delta \beta_1 \omega, \omega)}{D(\lambda + \Delta \beta_1 \omega, \omega)} \times e^{i(\omega\tau_0 - \lambda z)} d\lambda. \quad (4)$$

For large enough evolution, the integrals of Eq. (4) are dominated by the saddle point $\omega = \omega_s$ and $\lambda_s = \lambda(\omega_s)$ satisfying [30]

$$D(\lambda + \Delta \beta_1 \omega, \omega)|_{\omega_s} = 0, \quad \left. \frac{\partial D(\lambda + \Delta \beta_1 \omega, \omega)}{\partial \omega} \right|_{\omega_s} = 0. \quad (5)$$

Figure 1(a) represents the evolution of the output cavity spectra for a cavity mismatch ranging from -40 to $+40$ fs/m by

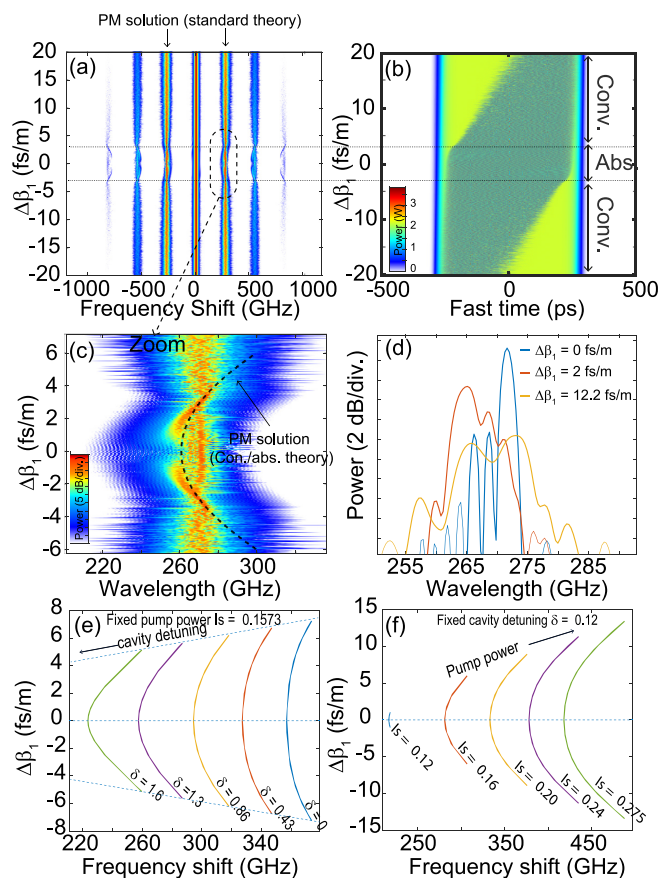


FIG. 1. (a) Evolution of the output spectrum as a function of the group velocity mismatch ($\Delta \beta_1$) from numerics [LLE integration, Eq. (1)]. (b) Evolution of the output power as a function of the group velocity mismatch. (c) Zoom on a MI sidelobe. The black dashed lines represent theoretical predictions from Eq. (3). (d) Zoom in on the MI sidelobe for different mismatch values (0, 2, 12 fs/m respectively from numerics). (e) and (f) Evolutions of the sidelobe positions and of the absolute regime zone as a function of the cavity detuning and the pump power, respectively, from theory [Eq. (3)]. With $\alpha = 0.2327$, $\theta = 0.05$, and $|E_{\text{in}}|^2 = 2.3$ W, extracted from experimental parameters which are all listed in Fig. 2's caption.

integrating the LLE (1) with the parameters corresponding to the experimental setup (see the list in Fig. 2's caption). For large cavity mismatch values (>5 fs/m), MI sidebands appear symmetrically on both sides of the pump. They are located at ± 270 GHz from the pump, in fairly good agreement with the standard (without $\Delta \beta_1$) steady state analysis predicting ± 274 GHz. At small cavity mismatch values [± 4 fs/m, see Fig. 1(c)], their positions vary as a function of $\Delta \beta_1$. The central frequency follows a parabola moving from 270 to 260 GHz for the minimum with a hole in the center (no mismatch) where the position comes back again at 270 GHz. This shows, against all odds, the MI sidelobe position depends on the first-order dispersion term that is not predicted from the standard linear stability analysis. It is also important to note their spectral widths are much narrower for weak mismatch values than for large ones [typically five times by considering the full width at half maximum (FWHM) values, see Fig. 1(d)]. This dynamics modification is due to the transition from an absolute regime to a convective one, as can be seen

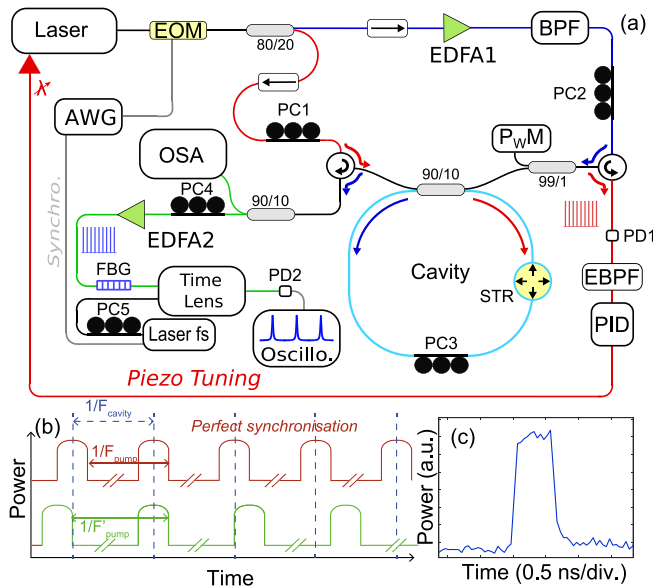


FIG. 2. (a) Experimental setup. EOM, electro-optical modulator; PC, polarization controller; PD, photodetector; OSA, optical spectrum analyzer; EDFA, erbium-doped fiber amplifier; BPF, bandpass filter; EBPF: electronic bandpass filter; STR: fiber stretcher; Laser fs: femtosecond laser; Oscillo., oscilloscope; PID, proportional-integrate-derivate controller; FBG, fiber Bragg grating; P_wM , power meter; AWG, arbitrary wave generator. Parameters: pulse width = 560 ps, $L = 27.44$ m, $\gamma = 2.5$ /W/km, $\beta_2 = -4.5$ ps²/km, finesse of 15.6, $P_p = 2.3$ W, $\Delta = 1$, and the zero mismatch repetition rate 7.431 555 16 MHz. (b) Cartoon illustrating the synchronization mismatch. The delay accumulated after one round trip when the pump pulse train has a synchronization mismatch with the cavity of $\Delta T = 1/F_{\text{pump}} - 1/F'_{\text{pump}}$. (c) Typical pump pulse from experimental recordings.

in Fig. 1(b), which showcases the output cavity temporal trace evolution. We recall that in the convective regime, localized perturbations grow but are shifted outside the system, whereas in the absolute regime, these drifting perturbations grow at any position on the top of the pump pulse and thus invade the entire pump pulse. When the perturbation invades the whole domain, for -4 fs/m $< \Delta\beta_1 < 4$ fs/m, the system evolves in an absolute regime. The position of the MI sidebands then depends on the cavity mismatch. On the contrary, in the convective regime, for $|\Delta\beta_1| > 4$ fs/m, instabilities drift toward the leading or trailing edges of the pump pulse depending on the mismatch sign, and eventually disappear (not shown here for the sake of clarity). Thus, the MI sideband position does not vary in that regime [Fig. 1(a)]. The variation of the sideband position in the absolute regime is calculated from Eq. (3). It is superimposed in Fig. 1(a) as black dotted lines. The agreement is fairly good, and the parabolalike evolution is well predicted by the theory. The absolute regime area is not predicted with a perfect quantitative agreement compared to numerical simulations (± 6 fs/m in theory against ± 4 fs/m in numerics). This may be due to the fact that nonlinear effects are not included in the linear space-time analysis. Indeed, the convective analysis assumes the power of the perturbation is weak compared to the pump power. Advanced analytical methods based on a multiscale analysis [24] could give a more

accurate quantitative description of the process, but this is beyond the scope of this paper. Indeed, we show on Fig. 1(c) a zoom on MI sidelobes where one may observe a halo around $\Delta\beta_1 = 0$. This halo is not reproduced by our theoretical analysis. Although this theory is a powerful mathematical tool for predicting spatiotemporal dynamics, it remains a linear approach. To account for the halo dynamics, a nonlinear theory is needed, which is out of the scope of this work. Furthermore, this phenomenon is less significant in comparison to the MI lobe modification we are interested in this paper. To get a deeper insight into the dynamics of the process, Figs. 1(e) and 1(f) represent the evolution of the sidelobe position and the absolute regime zone as a function of the cavity detuning and the pump power, respectively. In Fig. 1(e), we see the curvature of the parabola decreases with the cavity detuning together with an increase of the absolute regime zone. Considering an arbitrary observer moving with the velocity v in the laboratory frame, the global gain curve is obtained from $g(v) = \text{Im}[\lambda(\omega_s) - v\omega_s]$. The absolute zone corresponds to $g(v) > 0$, decreasing with the detuning. The impact of the pump power on the process reveals that for high peak power values [Fig. 1(f)], the absolute region size increases, as it is well known in convective systems. Furthermore, the size of the convective region [Fig. 1(b)] mostly depends on the noise characteristics of the system and can exist for larger mismatch values. This regime is not of interest in this study since we focus on changing the position of the MI sidelobes, which remains unchanged in this regime.

III. EXPERIMENTS

A. Experimental setup

The experimental setup is presented in Fig. 2. It is similar to the one described in Ref. [31]. It consists of a passive fiber ring cavity built with a specially designed dispersion-shifted fiber ($\beta_{\text{DSF}} = -4.5$ ps²/km at 1545 nm and $\gamma_{\text{DSF}} = 2.5$ W⁻¹ km⁻¹) closed by a 90/10 coupler made of the same fiber to get a perfectly uniform cavity of 27.44 m length with a finesse of 15.6. We drive the cavity with a train of square-shaped pulses of 560 ps duration [Fig. 2(c)]. This short pump duration prevents the buildup of stimulated Brillouin scattering by increasing the power threshold at which it appears [32,33]. Furthermore, it allows the generation of high peak power pulses to easily trigger nonlinear processes. These pulses are generated from a cw laser at 1545 nm (with a linewidth < 100 Hz) intensity modulated by an electro-optic modulator (EOM). The repetition rate of these pulses can be tuned owing to the arbitrary wave generator (AWG) driving the EOM. Pulses are then amplified by an erbium-doped fiber amplifier and filtered out by a narrow bandwidth filter (BPF, 100 GHz) to remove amplified spontaneous emission in excess. Finally, pump pulses are launched into the cavity through the right port of the cavity propagating in the anticlockwise direction (blue arrows). We launched one pulse per round trip. A fraction of the output power of the EOM is sent through the left port of the cavity, propagating in the clockwise direction (red arrows). This weak signal detected at the cavity output by a photodetector (PD1) provides an error signal for a feedback loop system (proportional-integrate-derivate) to

make the laser drift with the cavity. As in Ref. [15], a combination of three polarization controllers (PC1, 2, and 3) is used to control the cavity detuning (normalized detuning set to $\Delta = 1$, corresponding to a monostable regime [15]). The output cavity field is split into two arms at the output of a coupler, and the spectrum is analyzed with an optical spectrum analyzer (10% port), while successive ultrafast temporal traces are recorded in real time via a commercial time-lens system (Picoluz, Thorlabs). A fiber Bragg grating centered at the pump wavelength is used to attenuate the central spectral components (pump) that would saturate the time lens otherwise. The time stretching effect was obtained by pumping the time lens with a femtosecond laser centered at 1570 nm providing pulses with a fixed repetition rate of 99.88 MHz. This laser was used as a reference clock for all electronic devices of the setup. The magnified signal (magnified factor of 57) was recorded by a fast photodiode and an oscilloscope (70 GHz bandwidth each). With this time-lens system, we were able to record the real-time evolution of the output cavity field over a window of 40 ps with a resolution of about 300 fs. Figure 2(b) illustrates schematically the pump signal in the case of a perfectly synchronized cavity (red trace) and with a synchronization mismatch (green trace). As an example, a slight modification of the repetition rate of the pump of only 1 Hz leads to a synchronization delay of 19.8 fs (a synchronization mismatch of 0.7 fs/m). Thus, we used a highly stable frequency synthesizer to tune the repetition rate of several Hz only around a reference zero mismatch rep rate that we measured at 7.111 231 MHz (at 1545 nm).

B. Experimental results

The synchronization mismatch was tuned from -250 to $+250$ fs/m, corresponding to a variation of the repetition rate of 756 Hz. The cavity was pumped just above the cavity threshold. Figure 3(a) represents the evolution of the output cavity spectrum as a function of the synchronization mismatch ($\Delta\beta_1$). Over this synchronization mismatch range, we observe the emergence of the MI sidebands at about $+150$ fs/m and their disappearance at -150 fs/m. It means a mismatch of only ± 4.05 ps, about 0.7% of the pump duration, is enough to annihilate the coherent buildup of the MI process. Note that this behavior had also been observed in numerics, but the synchronization mismatch value at which it disappears is very hard to accurately predict. This is due to spurious interactions between noise and convective instabilities which leads to a modification of the instability threshold by sustaining the appearance of perturbations [34]. For a perfect synchronization mismatch ($\Delta\beta_1 = 0$), a set of two narrow symmetric sidebands (10 GHz at FWHM) located at 280 GHz from the pump are generated as well as two harmonics on each side [see a zoom on one sideband in Fig. 3(b), on the harmonics in Fig. 3(c), and the blue trace in Fig. 3(d)]. The MI spectra are almost symmetric with respect to the zero mismatch value [Fig. 3(a) is symmetric versus $\Delta\beta_1 = 0$]. The observed slight asymmetry is due to a slow drift of experimental parameters over the full acquisition time that exceeds 15 min. Therefore, we will restrict the description to the upper part of the figure ($\Delta\beta_1 > 0$) for simplicity. By slightly increasing the synchronization mismatch from $\Delta\beta_1 = 0$ to about 2 fs/m, the

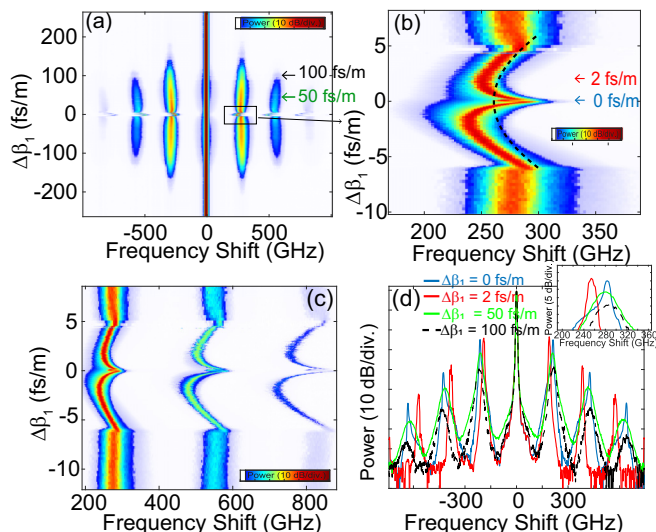


FIG. 3. (a) Two-dimensional (2D) plot of the output spectra as a function of the synchronization mismatch. (b) Zoom on the central part of the first sidelobe. (c) Zoom on the harmonics. (d) Output spectra for specific values of $\Delta\beta_1$ (0, 2, 50, and 100 fs/m). Inset: Zoom on the first sidelobe.

sideband position is shifted downward from 284 to 250 GHz [see also the blue and red curves in Fig. 3(d)] without noticeable lobe spectral broadening. By further increasing the synchronization mismatch, the center frequency increases to 280 GHz and the sidelobe width remains almost the same over the entire absolute region (± 5 fs/m). The theoretical predictions in dashed black lines [from Eq. (3)] are superimposed in Fig. 3(b). As can be seen, a fairly good agreement is obtained with the experiments. This confirms that the experimental observation of the modification of the MI sidelobe position is indeed due to the synchronization mismatch of the cavity. As explained in theory, the modification of the position of the MI sidebands is due to the gain and drift experienced by the perturbation in the absolute regime [see Fig. 1(b)]. In order to demonstrate the modification of the MI sideband position is indeed due to convective instabilities, we measured the drift of the MI pattern as a function of the cavity synchronization mismatch. The spatiotemporal evolution of the MI pattern had been recorded by using a time-lens system (see Fig. 2). It enabled us to observe the real-time evolution round trip to round trip of the output cavity pulse train of typically 4 ps period, with a high temporal resolution (300 fs). Five typical recordings of the real-time evolution round trip to round trip of the output cavity field are depicted in Figs. 4(a)–4(e). For a perfect synchronization mismatch shown in Fig. 4(c), MI patterns remain unchanged from round trip to round trip, leading to a stable perfectly vertical pattern in this 2D representation. The period is $\simeq 3.2$ ps, in fairly good agreement with the inverse of the sideband frequency shift ($1/272$ GHz $\simeq 3.6$ ps). For negative synchronization mismatch values, the MI pattern is left-tilted [Figs. 4(a) and 4(b)] while positive mismatch leads to right-tilted patterns [Figs. 4(d) and 4(e)]. Figure 4(f) shows the evolution of the drift velocity extracted from these measurements (plus additional ones not shown here) as a function of the synchronization mismatch, over a large synchronization

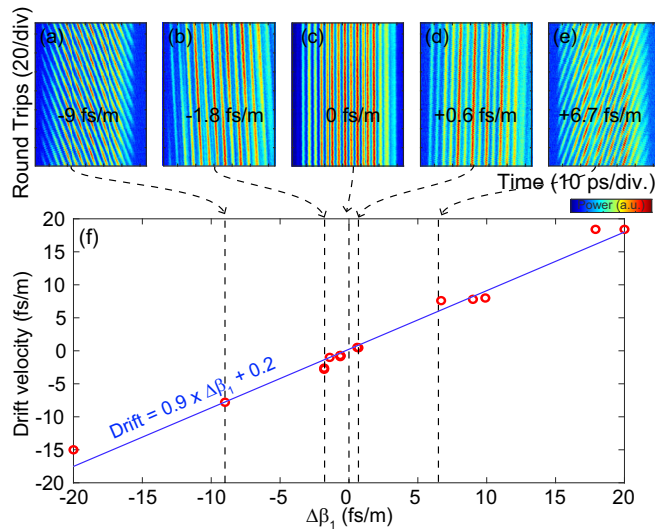


FIG. 4. (a)–(e) Round-trip to round-trip temporal trace evolution for three specific values of $\Delta\beta_1$ (-9 , -1.8 , 0 , 0.6 , and $+6.7$ fs/m). (f) Temporal drift of the pattern vs $\Delta\beta_1$.

mismatch span ($\Delta\beta_1 = \pm 20$ fs/m). A striking effect is that almost linear evolution from negative drifts to positive ones is observed with a slope of 0.9, which is very close to theoretical predictions [Eq. (3)], giving a slope of 1. This clearly highlights the crucial role of the propagation velocity induced by the pump-cavity synchronization mismatch.

IV. CONCLUSION

We reported the observation of the frequency shift of the modulation instability sidelobes due to the synchronization

mismatch between the pump and the resonator. We have shown that very small synchronization mismatches of a few Hz lead to a change in the position of the MI sidelobes when the system is operating in the absolute regime. Beyond this regime, the timing imbalance does not affect the shape or position of the bands until they disappear for larger values. These observations are in good agreement with numerical simulations as well as with theoretical predictions based on convection theory. The drift induced by the synchronization mismatch on the MI pattern is also observed in real time at the cavity exit using a temporal lens system. We have recorded pulse trains whose drift is proportional to the synchronization mismatch, in good agreement with theoretical predictions. These works provide a deeper understanding of the complex dynamics of the MI process in resonators. They revealed the unexpected contribution of the first-order dispersion term on the MI side lobe position, their harmonics, and thus Kerr combs in resonators. Further developments should lead to a detailed description of the impact of the synchronization mismatch on broader combs based on cavity solitons, corresponding to a higher nonlinear regime of MI [1].

ACKNOWLEDGMENT

This work was supported by the Agence Nationale de la Recherche (Programme Investissements d’Avenir FARCO project), Ministry of Higher Education and Research, Hauts de France Council (GPEG project), European Regional Development Fund (Photonics for Society P4S), the CNRS (IRP LAFONI) and H2020 Marie Skłodowska-Curie Actions (MSCA) (713694), and MEFISTA and University of Lille through the LAI HOLISTIC.

- [1] A. Pasquazi, M. Peccianti, L. Razzari, D. J. Moss, S. Coen, M. Erkintalo, Y. K. Chembo, T. Hansson, S. Wabnitz, P. Del’Haye, X. Xue, A. M. Weiner, and R. Morandotti, Micro-combs: A novel generation of optical sources, *Phys. Rep.* **729**, 1 (2018).
- [2] T. J. Kippenberg, A. L. Gaeta, M. Lipson, and M. L. Gorodetsky, Dissipative Kerr solitons in optical microresonators, *Science* **361**, eaan8083 (2018).
- [3] T. Herr, V. Brasch, J. D. Jost, C. Y. Wang, N. M. Kondratiev, M. L. Gorodetsky, and T. J. Kippenberg, Temporal solitons in optical microresonators, *Nat. Photonics* **8**, 145 (2014).
- [4] J. Li, J. Li, C. Bao, C. Bao, Q.-X. Ji, H. Wang, L. Wu, S. Leifer, C. Beichman, and K. Vahala, Efficiency of pulse pumped soliton microcombs, *Optica* **9**, 231 (2022).
- [5] E. Obrzud, S. Lecomte, and T. Herr, Temporal solitons in microresonators driven by optical pulses, *Nat. Photonics* **11**, 600 (2017).
- [6] M. Schmidberger, W. Chang, P. St. J. Russell, and N. Y. Joly, Influence of timing jitter on nonlinear dynamics of a photonic crystal fiber ring cavity, *Opt. Lett.* **37**, 3576 (2012).
- [7] M. H. Anderson, R. Bouchand, J. Liu, W. Weng, E. Obrzud, E. Obrzud, T. Herr, and T. J. Kippenberg, Photonic chip-based resonant supercontinuum via pulse-driven Kerr microresonator solitons, *Optica* **8**, 771 (2021).
- [8] I. Hendry, W. Chen, Y. Wang, B. Garbin, J. Javaloyes, G.-L. Oppo, S. Coen, S. G. Murdoch, and M. Erkintalo, Spontaneous symmetry breaking and trapping of temporal Kerr cavity solitons by pulsed or amplitude-modulated driving fields, *Phys. Rev. A* **97**, 053834 (2018).
- [9] I. Hendry, B. Garbin, S. G. Murdoch, S. Coen, and M. Erkintalo, Impact of desynchronization and drift on soliton-based Kerr frequency combs in the presence of pulsed driving fields, *Phys. Rev. A* **100**, 023829 (2019).
- [10] T. Daugey, C. Billet, J. Dudley, J.-M. Merolla, and Y. K. Chembo, Kerr optical frequency comb generation using whispering-gallery-mode resonators in the pulsed-pump regime, *Phys. Rev. A* **103**, 023521 (2021).
- [11] Y. Xu, Y. Xu, A. Sharples, A. Sharples, J. Fatome, J. Fatome, J. Fatome, S. Coen, S. Coen, M. Erkintalo, M. Erkintalo, S. G. Murdoch, and S. G. Murdoch, Frequency comb generation in a pulse-pumped normal dispersion Kerr mini-resonator, *Opt. Lett.* **46**, 512 (2021).
- [12] X. Xue, B. Yang, M. Wang, S. Li, X. Zheng, and B. Zhou, Dispersion-less Kerr solitons in spectrally confined optical cavities, *Light: Sci. Appl.* **12**, 19 (2023).

- [13] Y. Xu, Y. Xu, Y. Lin, A. Nielsen, A. Nielsen, I. Hendry, I. Hendry, S. Coen, S. Coen, M. Erkintalo, M. Erkintalo, H. Ma, H. Ma, S. G. Murdoch, S. G. Murdoch, and S. G. Murdoch, Harmonic and rational harmonic driving of microresonator soliton frequency combs, *Optica* **7**, 940 (2020).
- [14] M. Haelterman, S. Trillo, and S. Wabnitz, Dissipative modulation instability in a nonlinear dispersive ring cavity, *Opt. Commun.* **91**, 401 (1992).
- [15] S. Coen and M. Haelterman, Modulational Instability Induced by Cavity Boundary Conditions in a Normally Dispersive Optical Fiber, *Phys. Rev. Lett.* **79**, 4139 (1997).
- [16] M. Tlidi, A. Mussot, E. Louvergneaux, G. Kozyreff, A. G. Vladimirov, and M. Taki, Control and removal of modulational instabilities in low-dispersion photonic crystal fiber cavities, *Opt. Lett.* **32**, 662 (2007).
- [17] N. L. B. Sayson, T. Bi, V. Ng, H. Pham, L. S. Trainor, H. G. L. Schwefel, S. Coen, M. Erkintalo, and S. G. Murdoch, Octave-spanning tunable parametric oscillation in crystalline Kerr microresonators, *Nat. Photonics* **13**, 701 (2019).
- [18] F. Bessin, F. Copie, M. Conforti, A. Kudlinski, and A. Mussot, Modulation instability in the weak normal dispersion region of passive fiber ring cavities, *Opt. Lett.* **42**, 3730 (2017).
- [19] R. J. Briggs, *Electron-Stream Interaction with Plasmas* (MIT Press, Cambridge, MA, 1964).
- [20] H. Ward, M. N. Ouarzazi, M. Taki, and P. Glorieux, Influence of walkoff on pattern formation in nondegenerate optical parametric oscillators, *Phys. Rev. E* **63**, 016604 (2000).
- [21] N. Mitarai and H. Nakanishi, Spatiotemporal Structure of Traffic Flow in a System with an Open Boundary, *Phys. Rev. Lett.* **85**, 1766 (2000).
- [22] A. Couairon and J. M. Chomaz, Pattern Selection in the Presence of a Cross Flow, *Phys. Rev. Lett.* **79**, 2666 (1997).
- [23] A. Mussot, E. Louvergneaux, N. Akhmediev, F. Reynaud, L. Delage, and M. Taki, Optical Fiber Systems Are Convectively Unstable, *Phys. Rev. Lett.* **101**, 113904 (2008).
- [24] F. Leo, A. Mussot, P. Kockaert, P. Emplit, M. Haelterman, and M. Taki, Nonlinear Symmetry Breaking Induced by Third-Order Dispersion in Optical Fiber Cavities, *Phys. Rev. Lett.* **110**, 104103 (2013).
- [25] F. Leo, S. Coen, P. Kockaert, P. Emplit, M. Haelterman, A. Mussot, and M. Taki, Impact of third-order dispersion on nonlinear bifurcations in optical resonators, *Phys. Lett. A* **379**, 1934 (2015).
- [26] S. Coen, M. Tlidi, Ph. Emplit, and M. Haelterman, Convection versus Dispersion in Optical Bistability, *Phys. Rev. Lett.* **83**, 2328 (1999).
- [27] P. Parra-Rivas, D. Gomila, M. A. Matías, P. Colet, and L. Gelens, Effects of inhomogeneities and drift on the dynamics of temporal solitons in fiber cavities and microresonators, *Opt. Express* **22**, 30943 (2014).
- [28] M. Yu and C. J. McKinstrie, Impulse response of a nonlinear dispersive wave, *Phys. Rev. E* **52**, 6826 (1995).
- [29] S. Coulibaly, E. Louvergneaux, M. Taki, and L. Brevdo, Spatiotemporal wave-train instabilities in nonlinear Schrödinger equation: revisited, *Eur Phys. J. D* **69**, 186 (2015).
- [30] L. S. Hall and W. Heckrotte, Instabilities: Convective versus absolute, *Phys. Rev.* **166**, 120 (1968).
- [31] F. Bessin, F. Copie, M. Conforti, A. Kudlinski, A. Mussot, and S. Trillo, Real-Time Characterization of Period-Doubling Dynamics in Uniform and Dispersion Oscillating Fiber Ring Cavities, *Phys. Rev. X* **9**, 041030 (2019).
- [32] R. G. Smith, Optical power handling capacity of low loss optical fibers as determined by stimulated Raman and Brillouin scattering, *Appl. Opt.* **11**, 2489 (1972).
- [33] Y. Aoki, K. Tajima, and I. Mito, Input power limits of single-mode optical fibers due to stimulated Brillouin scattering in optical communication systems, *J. Lightwave Technol.* **6**, 710 (1988).
- [34] M. Santagiustina, P. Colet, M. San Miguel, and D. Walgraef, Noise-Sustained Convective Structures in Nonlinear Optics, *Phys. Rev. Lett.* **79**, 3633 (1997).